

The Sizes and Depletions of the Dust and Gas Cavities in the Transitional Disk J160421.7-213028

Ruobing Dong^{1,2}, Nienke van der Marel³, Jun Hashimoto⁴, Eugene Chiang², Eiji Akiyama⁵, Hauyu Baobab Liu⁶, Takayuki Muto⁷, Gillian R. Knapp⁸, Takashi Tsukagoshi⁹, Joanna Brown¹⁰, Simon Bruderer¹¹, Shin Koyamatsu¹², Tomoyuki Kudo¹³, Nagayoshi Ohashi⁴, Evan Rich¹⁴, Mayama Satoshi^{15,16}, Michihiro Takami¹⁷, John Wisniewski¹⁴, Yi Yang¹⁸, Zhaohuan Zhu¹⁹, Motohide Tamura^{4,12}

¹Steward Observatory, University of Arizona, Tucson, AZ, 85721, rdong@email.arizona.edu

²Department of Astronomy, University of California at Berkeley, 94720, Berkeley, CA

³Institute for Astronomy, University of Hawaii, Honolulu, HI 96822, marel@hawaii.edu

⁴Astrobiology Center, National Institutes of Natural Sciences, 2-21-1 Osawa, Mitaka, Tokyo 181-8588 Japan

⁵National Astronomical Observatory of Japan, 2-21-1, Osawa, Mitaka, Tokyo, 181-8588, Japan

⁶European Southern Observatory (ESO), Karl-Schwarzschild-Strasse 2, D-85748 Garching, Germany

⁷Division of Liberal Arts, Kogakuin University, 1-24-2 Nishi-Shinjuku, Shinjuku-ku, Tokyo 163-8677

⁸Department of Astrophysical Sciences, Princeton University, Princeton, NJ 08544

⁹College of Science, Ibaraki University, Bunkyo 2-1-1, Mito, Ibaraki 310-8512, Japan

¹⁰Boston Fusion

¹¹Max-Planck-Institut for Extraterrestrische Physik, Giessenbachstrasse 1, 85748 Garching, Germany

¹²Department of Astronomy, Graduate School of Science, The University of Tokyo, Hongo 7-3-1, Bunkyo-ku, Tokyo 113-0033, Japan

¹³Subaru Telescope, National Astronomical Observatory of Japan, 650 North Aohoku Place, Hilo, HI 96720, USA

¹⁴Homer L. Dodge Department of Physics, University of Oklahoma, Norman, OK 73071, USA

¹⁵The Center for the Promotion of Integrated Sciences, The Graduate University for Advanced Studies (SOKENDAI), Shonan International Village, Hayama-cho, Miura-gun, Kanagawa 240-0193, Japan

¹⁶Department of Astronomical Science, The Graduate University for Advanced Studies (SOKENDAI), 2-21-1 Osawa, Mitaka, Tokyo 181-8588, Japan

¹⁷Institute of Astronomy and Astrophysics, Academia Sinica, PO Box 23-141, Taipei 10617, Taiwan, ROC

¹⁸Department of Astronomical Science, The Graduate University for Advanced Studies, 2-21-1 Osawa, Mitaka, Tokyo 181-8588, Japan

¹⁹Department of Physics and Astronomy, University of Nevada, Las Vegas, 4505 South Maryland Parkway, Las Vegas, NV 89154

ABSTRACT

We report ALMA Cycle 2 observations of 230 GHz (1.3 mm) dust continuum emission, and ^{12}CO , ^{13}CO , and C^{18}O $J = 2-1$ line emission, from the Upper Scorpius transitional disk [PZ99] J160421.7-213028, with an angular resolution of $\sim 0''.25$ (35 AU). Armed with these data and existing H-band scattered light observations, we measure the size and depth of the disk’s central cavity, and the sharpness of its outer edge, in three components: sub- μm -sized “small” dust traced by scattered light, millimeter-sized “big” dust traced by the millimeter continuum, and gas traced by line emission. Both dust populations feature a cavity of radius ~ 70 AU that is depleted by factors of at least 1000 relative to the dust density just outside. The millimeter continuum data are well explained by a cavity with a sharp edge. Scattered light observations can be fitted with a cavity in small dust that has either a sharp edge at 60 AU, or an edge that transitions smoothly over an annular width of 10 AU near 60 AU. In gas, the data are consistent with a cavity that is smaller, about 15 AU in radius, and whose surface density at 15 AU is $10^{3\pm 1}$ times smaller than the surface density at 70 AU; the gas density grades smoothly between these two radii. The CO isotopologue observations rule out a sharp drop in gas surface density at 30 AU or a double-drop model as found by previous modeling. Future observations are needed to assess the nature of these gas and dust cavities, e.g., whether they are opened by multiple as-yet-unseen planets or photoevaporation.

Subject headings: protoplanetary disks — stars: pre-main sequence — stars: variables: T Tauri, Herbig Ae/Be — planets and satellites: formation — circumstellar matter — stars:individual ([PZ99] J160421.7-213028)

1. Introduction

Transitional disks are gaseous protoplanetary disks with a central depleted region¹ (see the review by Espaillat et al. 2014). They mark a crucial phase in disk evolution, intermediate between fully gas-rich and gas-depleted systems. Their existence was first suggested by the distinctive near-to-mid-infrared (NIR-MIR) dips in their spectral energy distributions (SEDs; e.g. Strom et al. 1989; Skrutskie et al. 1990; Calvet et al. 2005; Espaillat et al. 2007, 2008),

¹In the literature the central depleted region has been called a “gap” or a “cavity”, depending on whether the structure extends all the way to the star. In this paper we refer to the structure in J1604 as a cavity.

and later confirmed by resolved images in NIR scattered light (e.g., Thalmann et al. 2010; Hashimoto et al. 2012; Mayama et al. 2012; Garufi et al. 2013; Quanz et al. 2013; Avenhaus et al. 2014a,b; Tsukagoshi et al. 2014) and by resolved mm-wave maps of dust continuum and gas line emission (e.g. Andrews et al. 2011; Mathews et al. 2012; Tang et al. 2012; Isella et al. 2013; van der Marel et al. 2013; Fukagawa et al. 2013; van der Marel et al. 2014; Pérez et al. 2014; Zhang et al. 2014; van der Marel et al. 2015a; Canovas et al. 2015; Hashimoto et al. 2015).

What opens the cavities in transitional disks? This is still an open question. The leading hypothesis is dynamical sculpting by planets (or more massive companions) inside the cavity. Cavity opening is a natural outcome of tidal interactions between a disk and companions (e.g., Lin & Papaloizou 1993; Artymowicz & Lubow 1994; Bryden et al. 1999; Kley & Nelson 2012). While a single gap opened by one giant planet may be too narrow to account for the observed cavity sizes in the gas and scattered light, Zhu et al. (2011), Dodson-Robinson & Salyk (2011), and Dong et al. (2015) explored the possibility of opening a cavity by multiple giant planets (see also Duffell & Dong 2015). In this scenario, the sharpness of the gas cavity edge increases with planet mass (e.g., Duffell 2015). Large gradients in gas surface density can cause the appearance of the cavity (e.g., its size) to depend on wavelength. Because mm-sized dust particles can pile up at the pressure bump outside the gas cavity edge (this is called the “dust filtration” effect; Rice et al. 2006; Zhu et al. 2012; Pinilla et al. 2012b,a; de Juan Ovelar et al. 2013), cavities viewed in the mm continuum can be larger than they appear in scattered light and gas observations. Another consequence of cavity opening by companions is a reduced accretion rate onto the star, depending on how much of the disk accretion flow is diverted onto the companions. A small inner disk may remain if no companions are present there.

The main alternative non-planet mechanism for clearing big cavities in transitional disks is photoevaporation (e.g., Clarke et al. 2001; Owen et al. 2010, 2011; Suzuki et al. 2010). In this scenario, stellar radiation ionizes surface layers of the disk and launches a wind from the outer disk; if the disk accretion rate is smaller than the wind mass loss rate, the inner disk is starved and a cavity opens. In this scenario, the cavity edge in both gas and dust tends to be sharp (e.g., Alexander et al. 2006; Alexander & Armitage 2007), and since the disk is cleared from the inside out, the accretion on to the star is expected to be very low or zero (e.g., Owen et al. 2011). Particle trapping at the gap edge can also occur in photoevaporated cavities.

Other mechanisms for explaining large cavities in observations have also been proposed, such as grain growth (e.g., Birnstiel et al. 2012) and disk shadowing (e.g., Garufi et al. 2014, for cavity/ring structures seen in scattered light). However, these mechanisms cannot

reproduce certain observed features in the disks such as cavity edges (Birnstiel et al. 2012; Dong 2015).

Identifying the origin of the cavity has important implications for disk evolution and planet formation. Multi-wavelength, spatially resolved observations are needed, as various cavity formation mechanisms predict different structures for different components, resulting in different observed disk morphologies at different wavelengths. [PZ99] J160421.7-213028 (hereafter J1604), a transitional disk heavily scrutinized in recent years, provides an excellent case study. This nearly face-on (inclination $\sim 6^\circ$; Mathews et al. 2012) system is located at ~ 145 pc in the ~ 5 – 10 Myr old Upper Scorpius star forming region (de Zeeuw et al. 1999; Pecaute et al. 2012). The central source is a pre-main-sequence star with a spectral type of K2, an effective temperature of $T_{\text{eff}} \sim 4500\text{K}$, and a mass $M_\star \sim 1M_\odot$ (Dahm & Carpenter 2009; Mathews et al. 2012; Carpenter et al. 2014). Its cavity is one of the largest, extending to ~ 70 AU, as vividly revealed in NIR polarized light by Subaru/HiCIAO (H -band; Mayama et al. 2012) and VLT/SPHERE (R' -band; Pinilla et al. 2015). Millimeter observations using SMA (0.88 mm; Mathews et al. 2012) and ALMA (cycle0, 0.88 mm, band 7; Zhang et al. 2014) have resolved the cavity in dust and CO $J=3-2$ emission, with angular resolutions of $0''.51 \times 0''.34$ and $0''.73 \times 0''.46$, respectively. As a transitional disk, J1604 has several peculiar properties. In particular, Owen (2016) pointed out that most transitional disks can be classified into two classes: one with small holes ($\lesssim 10$ AU) and low accretion rates ($< 10^{-9}M_\odot \text{ yr}^{-1}$), and another with large holes ($\gtrsim 20$ AU) and high accretion rates $\sim 10^{-8}M_\odot \text{ yr}^{-1}$. J1604 belongs to neither: it has one of the largest holes, and yet it is hardly accreting (Mathews et al. 2012).

In this paper, we present new ALMA Cycle 2 Band-6 (1.3 mm) dust continuum and $J=2-1$ line observations for three CO isotopologues ($^{12}\text{CO}/^{13}\text{CO}/\text{C}^{18}\text{O}$), with an angular resolution of $\sim 0''.25$, the highest at mm wavelengths to date. These data, in combination with a well-sampled SED and resolved observations at $0.6 \mu\text{m}$, $1.6 \mu\text{m}$, and 0.88 mm, afford an unprecedentedly detailed examination of a transitional disk. We probe cavity structures in dust and gas using parametrized axisymmetric disk models and dust and line radiative transfer simulations (Section 3), to answer three basic questions (Section 4):

1. What are the sizes of the cavities seen in various disk components: “small” sub- μm -sized dust traced by scattered light, “big” millimeter-sized grains traced by mm dust continuum emission, and gas traced by CO?
2. How depleted are the cavities in the various disk components?
3. How sharp are the cavity edges in the various disk components?

A summary and discussion are given at the end (Section 5).

2. ALMA Observations and Data Reduction

J1604 (RA 16:04:21.643, Dec -21:30:28.72; Cutri 2013) was observed with the Atacama Large Millimeter/submillimeter Array (ALMA) in Band 6 (230 GHz) during ALMA Cycle 2 observations (program ID: 2013.1.01020.S, PI: T. Tsukagoshi) in July 2015. The observations were conducted in four spectral windows: two with bandwidths of 117.19 MHz (and channel widths of 61.035 kHz; equivalent to a velocity resolution of ~ 0.08 km s $^{-1}$) centered on ^{12}CO (2–1) and ^{13}CO (2–1); one with a bandwidth of 468.75 MHz (and a channel width of 0.244 MHz; equivalent to a velocity resolution ~ 0.33 km s $^{-1}$) centered on C^{18}O (2–1); and a fourth spectral window for continuum observations with a higher sensitivity bandwidth of 1875.00 MHz (and a channel width of 31.250 MHz). The flux and bandpass were calibrated with the quasar J1517-243, which was used as a bandpass calibrator as well. The gain/phase calibrator was quasar J1559-2442. The total on-source integration time was 316 seconds.

The data were calibrated with CASA (McMullin et al. 2007, version 4.2) following the calibration scripts provided by EA-ARC, and then imaged in CASA using the CLEAN algorithm (Rau & Cornwell 2011). The continuum data were concatenated from four spectral windows providing ~ 2.6 GHz of continuum bandwidth.

The continuum data were cleaned using Briggs weighting with a robust factor of 0.5, and the line data were cleaned using natural weighting, resulting in a beam size of $\sim 0''.25$. Natural weighting was chosen over Briggs weighting for the line data for better image recovery as the signal-to-noise ratio is lower for the line data.

The 230 GHz continuum emission and the three CO 2–1 isotopologues ^{12}CO (230.538 GHz), ^{13}CO (220.398677 GHz) and C^{18}O (219.56036 GHz) were all imaged. Table 1 summarizes the continuum and line data.

Figure 1 shows the continuum map, the zero-moment maps (total line intensity) for all three CO lines, and the first-moment map (the velocity field) in ^{12}CO 2–1. The continuum is detected with a peak signal-to-noise ratio of 36 ($\sigma=0.11$ mJy beam $^{-1}$), the integrated line intensities have a peak signal-to-noise ratio of 17, 9 and 6 for ^{12}CO , ^{13}CO and C^{18}O , respectively, with $\sigma_{\text{line}} \approx 11$ mJy km s $^{-1}$ for the integrated emission. The σ is determined by measuring the standard deviation in a ring outside a $2''$ radius in the continuum and zero-moment maps. The first-moment map is consistent with Keplerian rotation, and the stellar position derived from the first-moment map is RA 16 h 04 m 21.638 s , Dec -21 $^\circ$ 30'28.98", consistent with the position of the star in the optical/IR. We derive a position angle of 80°

and an inclination of 6° , consistent with previous estimates based on ALMA Cycle 0 data. The 230 GHz continuum image shows a narrow, azimuthally symmetric ring, as was found in previous observations at 345 GHz with lower spatial resolution (Mathews et al. 2012; Zhang et al. 2014; van der Marel et al. 2015b). The zero moment maps of the CO lines show rings as well, but with smaller inner radii than the continuum ring, again consistent with previous findings. Figure 2 shows the azimuthally averaged radial cuts for continuum and integrated line emission. The inner radii of the ^{13}CO and C^{18}O rings appear slightly larger than that of the ^{12}CO ring; this may be an effect of their optical depths differing according to their different abundances. The azimuthally averaged (after correcting for the small inclination) visibility profiles of both continuum and integrated CO data (bottom panels of Figure 1) are consistent with ring profiles as well: all profiles show clear nulls, at $\sim 130\text{ k}\lambda$ (continuum), $\sim 170\text{ k}\lambda$ (^{12}CO), $\sim 110\text{ k}\lambda$ (^{13}CO) and $\sim 110\text{ k}\lambda$ (C^{18}O).

Non-Keplerian motion may indicate the presence of fast radial flows or disk warps (e.g., Rosenfeld et al. 2014; Casassus et al. 2015), or turbulence caused by various instabilities (e.g., Simon et al. 2015; Flaherty et al. 2015). The ALMA observations of J1604 do not show any clear indications of non-Keplerian motions, but the nearly face-on orientation of the disk makes velocity determinations difficult.

3. Modeling

Protoplanetary disks contain gas and variously sized dust grains. Dust dominates the opacity at nearly all continuum wavelengths. For the purpose of modeling observations, a disk may be approximated as a three-component system, each primarily responsible for observations in one wavelength range (e.g., Dong et al. 2012b; van der Marel et al. 2015b): (1) gas — vertically supported by pressure, producing CO emission; (2) sub-micron-sized dust (hereafter “small” dust) — generally well-mixed with gas in the vertical direction and mainly responsible for the NIR scattered light; and (3) $\sim\text{mm}$ -sized grains (hereafter “big” dust) — possibly concentrated in regions of high gas pressure including the disk midplane (Dullemond & Dominik 2004; D’Alessio et al. 2006; Birnstiel et al. 2010), and mainly responsible for mm continuum emission. The distribution of small dust grains does affect the mm continuum by regulating the disk temperature (starlight is intercepted and reprocessed first by small dust at large altitude); however, this dependence of the mm-wave map on small dust is relatively minor: midplane temperatures at a given radius vary by a factor of a few at most using different dust distributions, while surface densities in all three disk components vary by several orders of magnitudes across the cavity, as we will show.

We use radiative transfer simulations and parametrized disk models to produce synthetic

observations and compare them with the data. The models are axisymmetric with as few radial parameters as needed to match the observations. We do not aim at formally fitting the observations in a χ^2 manner, as this is impractical given the large number of degrees of freedom; fitting is done by eye instead. We are interested in obtaining rough estimates for basic properties of the cavity (as viewed in each component): the cavity size, degree of depletion, and the sharpness of its edge. We employ two radiative transfer tools to produce synthetic observations. For scattered light, we use the Whitney et al. (2013) Monte Carlo radiative transfer (MCRT) code; for dust continuum and CO line emission, we use the physical-chemical DALI code (Bruderer et al. 2012; Bruderer 2013). We treat the small dust separately from the big dust and the gas in the modeling, and largely follow the procedures described by Dong et al. (2012a) for scattered light and van der Marel et al. (2016) for mm continuum and line emission.

The disk starts from the dust sublimation radius R_{sub} , corresponding to a temperature of ~ 1500 K (~ 0.055 AU for J1604), and extends to an outer radius R_{out} . For the central source, we use a pre-main sequence star of spectral type K2, radius $1.4 R_{\odot}$, mass $1.0 M_{\odot}$, and temperature 4500 K. The star is not known to be accreting ($\dot{M} < 10^{-11} M_{\odot}/\text{yr}$; Mathews et al. 2012). Our model’s surface density profile $\Sigma(R)$ divides into an outer disk and a depleted inner disk for all three components, as illustrated in Figure 3:

$$\Sigma(R) = \begin{cases} \delta_{\text{cav}}(R)\Sigma_0 \left(\frac{R_c}{R}\right)^\gamma e^{-R/R_c}, R \leq R_{\text{cav}} & \text{Cavity} \\ \Sigma_0 \left(\frac{R_c}{R}\right)^\gamma e^{-R/R_c}, R_{\text{cav}} < R \leq R_{\text{out}} & \text{Outer Disk} \end{cases} \quad (1)$$

where the exponential length scale R_c , power-law index γ , cavity depletion factor $\delta_{\text{cav}}(R)$, and cavity radius R_{cav} are parameters specific to each of the three disk components (small dust, big dust, and gas). For small dust we introduce an additional rim structure from R_{sub} to R_{rim} to account for possible NIR excess:² the surface density of small dust inside the rim is given by $\delta_{\text{rim}}\Sigma_0 \left(\frac{R_c}{R}\right)^\gamma e^{-R/R_c}$. Note that δ_{cav} can vary with radius. In some of our models we will set δ_{cav} to be constant, while in others we will allow it vary with radius to introduce additional structure.

In the vertical direction z , strongly irradiated (i.e., passive) protoplanetary disks are roughly isothermal, except in the tenuous upper layers (Chiang & Goldreich 1997; Dullemond

²J1604 has been labeled a possible variable source by Dahm & Carpenter (2009); the IRAC data indicate no NIR excess, while the Spitzer IRS spectrum indicate a NIR excess. The later WISE data at 3.4 and 4.6 μm (Cutri 2012) are consistent with the IRS spectrum but not the IRAC photometry. We adopt the WISE and IRS data in this paper (the IRAC data are not plotted in Figure 3).

2002). In hydrostatic equilibrium, the vertical gas density follows a Gaussian profile:

$$\rho(R, z) = \frac{\Sigma(R)}{\sqrt{2\pi}h} e^{-z^2/2h^2}, \quad (2)$$

where h is the scale height. The big grains tend to settle to the midplane; we assume their vertical distribution also obeys a Gaussian but with a smaller h . Radially, the scale height is assumed to vary with radius as

$$h \propto R^\psi, \quad (3)$$

where ψ is a component-dependent constant.

We adopt the interstellar medium dust model of Kim et al. (1994) for small dust (composed of silicate, graphite, and amorphous carbon) with a size distribution that runs from $\sim 0.002\mu\text{m}$ to $\sim 0.25\mu\text{m}$. As J1604 is nearly face-on, the scattering angle everywhere in the scattered light image is close to 90° . We assume the Andrews et al. (2011) big dust model for our big dust, which has a minimum size of $0.005\mu\text{m}$ and a maximum size of 1mm with a power law differential size (s) distribution $n(s) \propto s^{-3.5}$. Mie scattering is assumed for both dust populations.

For the modeling of the CO isotopologues, the DALI code (Bruderer et al. 2012; Bruderer 2013) is used. DALI is a physical-chemical modeling code which solves the heating-cooling balance of the gas and chemistry simultaneously to determine the gas temperature, molecular abundances and molecular excitation in every position in the disk for a given density structure. DALI uses a chemical reaction network of about 110 species and 1500 reactions, including basic grain-surface reactions (freeze-out, sublimation and hydrogenation). DALI is required for proper interpretation of CO emission for several reasons: the gas and dust temperature are decoupled in disks, especially inside and at the cavity edges; the local CO abundance w.r.t. H_2 is lowered due to photodissociation and freeze-out and is thus not a direct gas density tracer; CO is formed and destroyed through various chemical reactions depending on the local conditions in the disk. DALI has been used to interpret several transition disks in spatially resolved CO observations (Bruderer et al. 2014; van der Marel et al. 2015b, 2016). The full details on the DALI model are discussed in these papers as well. The assumed abundance ratios of the CO isotopologues in DALI are $^{12}\text{CO}/^{13}\text{CO}=77$ and $^{12}\text{CO}/\text{C}^{18}\text{O}=560$. The effects of isotope-selective photodissociation (e.g., Miotello et al. 2014) have been checked but these do not significantly change the emission for our fiducial model.

In total, there are 23 parameters: Σ_0 (equivalent to the total disk mass), R_c , R_{out} , γ , ψ , R_{cav} , and δ_{cav} for each of the 3 components, plus δ_{rim} and R_{rim} for the small dust. We use subscripts “gas,” “small-dust,” and “big-dust” to indicate each component. We

are mainly interested in the cavity size, depletion, and edge structure for each of the three components. These parameters largely determine the cavity morphology in observations, while experiments have shown that our data are insensitive to many of the other parameters (Dong et al. 2012b,a; van der Marel et al. 2015b, 2016).

From our model we generate the SED, and images in H -band polarized light, mm continuum, and $^{12}\text{CO}/^{13}\text{CO}/\text{C}^{18}\text{O}$ $J=2-1$ emission. For scattered light we use the Subaru/HiCIAO image by Mayama et al. 2012 (data taken as part of the SEEDS planet and disk survey; Tamura 2009), and for continuum and line emission we use the ALMA Cycle 2 data presented in this paper. For the H -band images, we convolve the full resolution model images with the observed HiCIAO point spread function to achieve the appropriate angular resolution. Synthetic ALMA images are convolved with the ALMA angular resolution as given in Table 1. Also, we calculate the visibility profiles directly from the integrated gas moment maps and continuum images and compare these with the observed visibility profiles.

4. Disk Properties

In this section, we first present a fiducial model that fits all the observations reasonably well (Section 4.1). We then vary the sizes (4.2), depletion factors (4.3), and sharpnesses of the cavity edges (4.4) to explore the uncertainties.

4.1. The Fiducial Model

Table 2 lists the parameters of the fiducial model as portrayed in Figures 3–6. Figure 3 shows the model surface density radial profiles for the three components and compares the global SED of the model with observations. Figure 4 compares the H-band polarized intensity images; Figure 5 the visibilities of the models and data for the line emission and mm continuum; and Figure 6 the model and observed maps for the same. The photometry and the *IRS* spectrum used to construct the SED are listed in Table 3. The fiducial model qualitatively reproduces the SED, the image morphology at each wavelength, the radial profile of the scattered light, the mm visibilities, and the CO spectrum (none of the synthetic observations has been rescaled in flux). The fiducial model is also consistent with ALMA Cycle 0 345 GHz continuum and ^{12}CO $J=3-2$ data (not shown).

The total dust mass in the model is $0.066 M_{\text{J}}$ ($0.013 M_{\text{J}}$ in small dust and $0.053 M_{\text{J}}$ in big dust), and the total gas mass is $2.5 M_{\text{J}}$, resulting in a global gas-to-dust-mass ratio of $\sim 38:1$. The scattered light and dust continuum observations are consistent with the

simplest model — an outer disk, a cavity that is completely empty (except possibly for a < 0.1 AU inner disk in small dust, see below), and a sharp cavity edge. For the small dust we have an inner rim extending from $R_{\text{sub}} = 0.055$ AU to $R_{\text{rim}} = 0.07$ AU, included to account for the occasional NIR excess (see footnote 2). Note that detailed SED fitting is beyond the scope of this paper. In reality grain sizes can vary across the disk, and relaxing our assumption of a single grain size distribution can help on the SED fitting. This inner rim does not affect the three resolved observations discussed here. The cavity sizes in the two dust populations differ slightly ($R_{\text{cav,small-dust}} = 60$ AU while $R_{\text{cav,big-dust}} = 70$ AU); however, we will see later that the difference is insignificant. For the gas, the simple cavity model — a gas cavity of 30 AU with a sharp edge, used by van der Marel et al. (2015b) to fit the lower resolution Cycle 0 ^{12}CO data — does not fit the new ALMA ^{13}CO and C^{18}O data (Section 4.4). In order to fit all three isotopologues simultaneously, a smooth rather than a sharp cutoff at the gas cavity edge is required. We therefore add to the fiducial model for gas by introducing a smooth exponential drop-off in surface density between the big-dust cavity radius $R_{\text{cav,big-dust}} = 70$ AU and the gas cavity radius $R_{\text{cav,gas}} = 15$ AU. A full description of the gas surface density in the fiducial model is:

$$\Sigma_{\text{gas}}(R) = \begin{cases} \delta_{\text{cav,gas}}(R) \Sigma_{0,\text{gas}} \left(\frac{R_{\text{c,gas}}}{R} \right)^{\gamma_{\text{gas}}} e^{-R/R_{\text{c,gas}}} & R \leq R_{\text{cav,gas}} \text{ Cavity} \\ \Sigma_{\text{gas}}(R_{\text{cav,big-dust}}) \cdot e^{(R-R_{\text{cav,big-dust}})/w} & R_{\text{cav,gas}} \leq R \leq R_{\text{cav,big-dust}} \text{ Transition Region} \\ \Sigma_{0,\text{gas}} \left(\frac{R_{\text{c,gas}}}{R} \right)^{\gamma_{\text{gas}}} e^{-R/R_{\text{c,gas}}} & R_{\text{cav,big-dust}} \leq R \leq R_{\text{out,gas}} \text{ Outer Disk} \end{cases} \quad (4)$$

where w is

$$w = \frac{R_{\text{cav,big-dust}} - R_{\text{cav,gas}}}{\ln[\Sigma_{\text{gas}}(R_{\text{cav,big-dust}})/\Sigma_{\text{gas}}(R_{\text{cav,gas}})]}. \quad (5)$$

As a point of clarification, the free parameters in the above equations are $\delta_{\text{cav,gas}}$, $\Sigma_{0,\text{gas}}$, $R_{\text{c,gas}}$, γ_{gas} , $R_{\text{cav,gas}}$, and $R_{\text{cav,big-dust}}$. We connect the gas surface density to $R_{\text{cav,big-dust}}$ so that the gas pressure reaches a local maximum there — see Figure 3. This is motivated by dust filtration, which predicts that mm-sized particles drift toward the pressure peak. Inside $R_{\text{cav,gas}}$, $\delta_{\text{cav,gas}} = 10^{-5}$ — note that this implies the gas surface density at 15 AU is about 10^{-3} of the value at 70 AU. The gas-to-dust ratio is 50:1 in the outer disk. We note that our fiducial model overproduces the ^{13}CO and C^{18}O emission in the outer disk (at the shortest baselines) compared to the data, but we do not consider this discrepancy further as our focus in this paper is on the inner cavity.

We emphasize that the fiducial model does not provide a unique fit to the data. With the exceptions of cavity radius and depth, as discussed below, the constraints on many other parameters are rather weak (e.g., Dong et al. 2012a,b; van der Marel et al. 2015b). Also, local non-axisymmetric features, such as the dip on the ring at H -band, are not reproduced

and are beyond the scope of this paper.

4.2. How Big are the Cavities?

To illustrate the effect of cavity size on various observations, we show models with 3 cavity sizes for each disk component — 50, 60, and 70 AU for $R_{\text{cav,small-dust}}$ (Figure 7), 60, 70, and 80 AU for $R_{\text{cav,big-dust}}$, and 5, 15, and 25 for $R_{\text{cav,gas}}$ (Figure 8). We focus on resolved observations as the SED only weakly depends on the cavity sizes within the range of our parameter exploration (Figure 9; the same is true for the discussions in Sections 4.3 and 4.4). We observe the following:

- In scattered light, setting $R_{\text{cav,small-dust}} = 50$ AU (70 AU) results in a cavity too small (too large) to be consistent with the observations. The root-mean-square scatter of the observed H -band radial profile can roughly tolerate a ± 5 AU deviation from the fiducial model value of $R_{\text{cav,small-dust}} = 60$ AU, assuming a sharp cavity edge.
- In the dust continuum, a smaller (bigger) cavity in the big dust pushes the nulls on the visibility curve towards longer (shorter) deprojected baselines. The data are roughly consistent with $R_{\text{cav,big-dust}} = 70 \pm 10$ AU.
- In CO emission, the shape of the visibility profile around the null changes noticeably when the cavity size is changed. The cavity size in gas is roughly $R_{\text{cav,gas}} = 15 \pm 10$ AU.

We conclude that the gas cavity is much smaller than the dust cavity, while the cavity in the small dust is marginally smaller than in the big dust.

4.3. How Deep are the Cavities?

Varying the cavity depletion has dramatic effects:

- In scattered light, increasing $\delta_{\text{cav,small-dust}}$ smooths the ring and raises the surface brightness inside the cavity, as illustrated in Figure 10. For these extra models, $\Sigma_{\text{cav,small-dust}}$ is depleted to 10^{-2} , 10^{-3} , and 10^{-4} of its value at the cavity edge, and smoothly joins the fixed rim at 0.07 AU with $\delta_{\text{cav,small-dust}} = 10^{-6}$ in order to match the SED; at $R > 10$ AU, δ_{cav} is nearly constant, i.e., $\delta_{\text{cav,small-dust}}(R) \approx \delta_{\text{cav,small-dust}}(R = 60 \text{ AU})$. To be consistent within error bars with the Subaru data—in particular to

reproduce the contrast of the cavity—the drop in small dust surface density beyond 10 AU needs to be at least a factor of 1000; indeed the data are consistent with no small dust at all, as in the fiducial model.

- In the millimeter dust continuum, a depletion in the big dust of less than 1000 results in excess emission in the center of the image and a vertical offset in the visibility curve. The data are consistent with no big dust at all. Thus we conclude $\delta_{\text{cav, big-dust}} \leq 10^{-3}$.
- In CO emission, the visibility data and null positions appear to constrain $\delta_{\text{cav, gas}}$ to within a factor of 10 of our fiducial value.

We conclude that the gas cavity is shallower than the small-dust and big-dust cavities. The constraints on the cavity size and depth are summarized in Table 4 (assuming fiducial edge sharpnesses).

4.4. How Sharp are the Cavity Edges?

In this section, we explore “smooth” cavity edge structures in small and big dust, for which the transition from the cavity region to the outer disk occurs over a finite radius range. This profile is motivated by the shapes of the cavities in planet-disk interaction models (e.g., Duffell 2015; Fung & Chiang 2016). A key question is whether the big and small dust grains might have cavity edges having different shapes. There are many ways to model smooth cavity edges, and we restrict the discussion to a few illustrative cases. For the gas distribution, we show the effect of having a sharp cavity edge, and show that a smooth cavity edge is demanded by the CO observations.

- Figure 12 shows three models for the scattered light where transition regions from 60 to 70 AU are constructed to join the inner and outer disk in small dust. Introducing these smooth structures widens the cavity edge in scattered light. In addition, the ring shifts outward with a more abrupt transition at 70 AU and a smoother transition at 60 AU, as the 70 AU break gradually becomes the “new” cavity edge; the structures in scattered light trace the most abrupt changes in dust surface density. Overall, all the models considered appear consistent with the data.
- Figure 13 shows that a smooth drop in the big-dust distribution shifts the peak in the mm continuum emission toward smaller radius, and the model does not match the data at large baselines. Thus a smooth cavity edge in big dust appears inconsistent with the data.

- In gas observations, van der Marel et al. (2015b) successfully fitted the ALMA Cycle 0 ^{12}CO $J = 3-2$ observations with a sharp gas cavity edge at 30 AU; however, this model cannot fit the new ALMA CO data. As shown in Figure 13, a sharp drop-off at $R_{\text{cav,gas}} = 30$ AU gives model visibility profiles of the other CO isotope lines that have clear deviations around the location of the null (although the total integrated flux is similar and the ^{12}CO 2-1 visibility profile fits reasonably well). Also, a double-drop model (two sharp Σ_{gas} drops, one at $R_{\text{cav,big-dust}}$, the other at $R_{\text{cav,gas}}$), such as proposed by van der Marel et al. (2016), is not able to reproduce the visibility profiles of the CO isotope lines.

We conclude that the current data in scattered light cannot distinguish a sharp cavity edge from a smooth transition that takes places over 10 AU in the vicinity of the cavity edge, whereas the mm continuum data appear to require a relatively sharp cavity edge. The cavity edge structures in big and small dust can be approximately co-spatial. By comparison, the CO line data demand a smooth transition in gas density between 15 and 70 AU. Models with smooth gas cavity edges as in the fiducial model were also fitted successfully to previous CO isotopologue data of other transitional disks at lower spatial resolution (van der Marel et al. 2016).

5. Summary and Discussion

In this paper, we report on ALMA Cycle 2 observations of the transitional disk J160421.7-213028 (J1640) in 230 GHz continuum and ^{12}CO , ^{13}CO , and C^{18}O $J = 2-1$ emission. Using radiative transfer simulations, we construct a simple disk+cavity model to account for the spectral energy distribution (SED), and for resolved observations of the system in near-infrared (NIR) scattered light, dust continuum emission, and CO line emission. We constrain the radius of the cavity, its depth, and the sharpness of its edge. Our main results are as follows:

1. Our fiducial model, which fits the observations adequately by eye, has a completely empty cavity in both sub- μm -sized small dust and mm-sized big dust,³ of radius of 60–70 AU. The gas exhibits a cavity 15 AU in radius that is uniformly depleted by a factor of 10^5 ; the gas surface density grades smoothly from the edge of this gas cavity to the outer (undepleted) disk at 70 AU.

³Apart from a possible sub-0.1 AU dusty inner rim needed to account for a variable NIR excess.

2. The NIR scattered light observations constrain the cavity radius in small dust to within ± 5 AU from the best-fit value of 60 AU. The first null on the visibility curves of the dust continuum and C^{18}O emission constrain the cavity size in the big dust and in the gas to within ± 10 AU of 70 AU and 15 AU, respectively. Thus the data are consistent with the same cavity size in the two dust populations, while both dust cavities are significantly larger than the gas cavity.
3. While the scattered light and mm continuum data are consistent with a completely empty cavity in both small and big dust, the data can tolerate a finite factor of 10^3 depletion in both. The CO line data require gas surface densities at 15 AU to be depleted by factors of 10^2 – 10^4 relative to gas surface densities at 70 AU.
4. Currently, the NIR data cannot distinguish between a sharp cavity edge in the small dust population and a transition region of annular width 10 AU. The CO observations demand that gas densities vary smoothly inside 70 AU; a sharp gas cavity edge at 30 AU, or a model that drops in gas surface density at both 15 AU and 70 AU, cannot fit the data.

What is the nature of J1604’s cavity? J1604 bears a number of characteristics common to other transitional disks. It shows clear signs of a depleted inner region in all disk components, with a gas cavity that is substantially smaller than the dust cavity. Similar structures have been seen in a few transitional disks (van der Marel et al. 2015b, 2016), and are interpreted as evidence of dynamical clearing by (multiple) planets inside the cavities, coupled with dust filtration (e.g., Pinilla et al. 2012a; Zhu et al. 2012).

On the other hand, J1604 is unique among its peers in several ways. While all the other sources in the van der Marel ALMA CO disk sample have accretion rates on the order of $10^{-9}M_{\odot} \text{ yr}^{-1}$, J1604 has little accretion, no larger than $10^{-11}M_{\odot} \text{ yr}^{-1}$ (Dahm & Carpenter 2009; Dahm et al. 2012; Mathews et al. 2012). Furthermore, its innermost dust disk of radius ~ 0.1 AU may be time variable, with IRAC data indicating no NIR excess and the WISE photometry and Spitzer IRS spectrum indicating a small NIR excess (Table 3). In addition, while many transitional disks appear to be asymmetric in the ALMA dust continuum (e.g., van der Marel et al. 2013; Casassus et al. 2013; Pérez et al. 2014), J1604 has a nearly symmetric ring in thermal emission. At the same time, scattered light imaging shows that the ring has a small gap of time-varying position angle along its circumference (Mayama et al. 2012; Pinilla et al. 2015) — see Figure 4.

As discussed in Section 1, both dynamical sculpting by planets and photoevaporation can open cavities in disks. The main observational distinction between the two is whether the system still has significant accretion onto the central star. Transitional disks with signif-

icant accretion (on the order of $10^{-9}M_{\odot} \text{ yr}^{-1}$) may be compatible with planets, while those with negligible accretion may indicate starvation by photoevaporation (e.g., Alexander & Armitage 2009; Cieza et al. 2012; Owen & Clarke 2012; Espaillat et al. 2014). The observed small-to-zero accretion rate in J1604 suggests the latter. However, the smooth gas gap edge transition in J1604 appears inconsistent with photoevaporation (Section 1; e.g., Alexander & Armitage 2007), even as the small dust grains—which are expected to be well coupled to the gas—do exhibit a relatively sharp drop in density at the cavity edge. The difference between the small dust and gas edge structures is intriguing and merits future study. Finally, we note that if planets are responsible for opening the cavity, the size and depth of the cavity imply a chain of multiple massive planets, likely of multi-Jupiter masses, unless the disk viscosity α is substantially lower than 10^{-3} (Fung et al. 2014; Dong & Dawson 2016). Such planets at large radius have been found to be rare (Bowler 2016).

There are at least two paths forward for exploring the origin of the cavity in J1604. First, if the cavity is opened by (multiple) giant planets, these may be detected in deep direct imaging observations. So far the deepest exposure for J1604 is by Canovas et al. (2016), in which no planet candidates were found, and objects of mass 2–3 M_J outside 25 AU have been ruled out according to the hot-start planet formation model. Second, if the disk is currently being photoevaporated, blueshifted optical and infrared forbidden lines indicating a photoevaporative wind may be detectable in this nearly face-on system (see the example in TW Hya, Pascucci et al. 2011). Further observations are needed to elucidate the nature of J1604’s cavities.

Acknowledgments

We are grateful to the anonymous referee for constructive suggestions that improved the quality of the paper. This project is partially supported by NASA through Hubble Fellowship grant HST-HF-51320.01-A (R.D.) awarded by the Space Telescope Science Institute, which is operated by the Association of Universities for Research in Astronomy, Inc., for NASA, under contract NAS 5-26555. Numerical calculations were performed on the SAVIO cluster provided by the Berkeley Research Computing program, supported by the UC Berkeley Vice Chancellor for Research and the Berkeley Center for Integrative Planetary Science. This paper makes use of the following ALMA data: ADS/JAO.ALMA#2013.1.01020S. ALMA is a partnership of ESO (representing its member states), NSF (USA) and NINS (Japan), together with NRC (Canada), NSC and ASIAA (Taiwan), and KASI (Republic of Korea), in cooperation with the Republic of Chile. The Joint ALMA Observatory is operated by ESO, AUI/NRAO and NAOJ. The National Radio Astronomy Observatory is a facility

of the National Science Foundation operated under cooperative agreement by Associated Universities, Inc.

REFERENCES

- Alexander, R. D., & Armitage, P. J. 2007, *MNRAS*, 375, 500
- . 2009, *ApJ*, 704, 989
- Alexander, R. D., Clarke, C. J., & Pringle, J. E. 2006, *MNRAS*, 369, 229
- Andrews, S. M., Wilner, D. J., Espaillat, C., Hughes, A. M., Dullemond, C. P., McClure, M. K., Qi, C., & Brown, J. M. 2011, *ApJ*, 732, 42
- Artymowicz, P., & Lubow, S. H. 1994, *ApJ*, 421, 651
- Avenhaus, H., Quanz, S. P., Meyer, M. R., Brittain, S. D., Carr, J. S., & Najita, J. R. 2014a, *ApJ*, 790, 56
- Avenhaus, H., Quanz, S. P., Schmid, H. M., Meyer, M. R., Garufi, A., Wolf, S., & Dominik, C. 2014b, *ApJ*, 781, 87
- Bessell, M. S., Castelli, F., & Plez, B. 1998, *A&A*, 333, 231
- Birnstiel, T., Andrews, S. M., & Ercolano, B. 2012, *A&A*, 544, A79
- Birnstiel, T., Dullemond, C. P., & Brauer, F. 2010, *A&A*, 513, A79
- Bowler, B. P. 2016, ArXiv e-prints
- Bruderer, S. 2013, *A&A*, 559, A46
- Bruderer, S., van der Marel, N., van Dishoeck, E. F., & van Kempen, T. A. 2014, *A&A*, 562, A26
- Bruderer, S., van Dishoeck, E. F., Doty, S. D., & Herczeg, G. J. 2012, *A&A*, 541, A91
- Bryden, G., Chen, X., Lin, D. N. C., Nelson, R. P., & Papaloizou, J. C. B. 1999, *ApJ*, 514, 344
- Calvet, N., et al. 2005, *ApJ*, 630, L185
- Canovas, H., et al. 2016, ArXiv e-prints

- . 2015, *ApJ*, 805, 21
- Carpenter, J. M., Mamajek, E. E., Hillenbrand, L. A., & Meyer, M. R. 2006, *ApJ*, 651, L49
- Carpenter, J. M., Ricci, L., & Isella, A. 2014, *ApJ*, 787, 42
- Casassus, S., et al. 2015, *ApJ*, 811, 92
- . 2013, *Nature*, 493, 191
- Chiang, E. I., & Goldreich, P. 1997, *ApJ*, 490, 368
- Cieza, L. A., Schreiber, M. R., Romero, G. A., Williams, J. P., Rebassa-Mansergas, A., & Merín, B. 2012, *ApJ*, 750, 157
- Clarke, C. J., Gendrin, A., & Sotomayor, M. 2001, *MNRAS*, 328, 485
- Cohen, M., Wheaton, W. A., & Megeath, S. T. 2003, *AJ*, 126, 1090
- Cutri, R. M., et al. 2003, *VizieR Online Data Catalog*, 2246
- Cutri, R. M. e. 2013, *VizieR Online Data Catalog*, 2328
- Cutri, R. M. e. a. 2012, *VizieR Online Data Catalog*, 2311
- Dahm, S. E., & Carpenter, J. M. 2009, *AJ*, 137, 4024
- Dahm, S. E., Slesnick, C. L., & White, R. J. 2012, *ApJ*, 745, 56
- D’Alessio, P., Calvet, N., Hartmann, L., Franco-Hernández, R., & Servín, H. 2006, *ApJ*, 638, 314
- de Juan Ovelar, M., Min, M., Dominik, C., Thalmann, C., Pinilla, P., Benisty, M., & Birnstiel, T. 2013, *A&A*, 560, A111
- de Zeeuw, P. T., Hoogerwerf, R., de Bruijne, J. H. J., Brown, A. G. A., & Blaauw, A. 1999, *AJ*, 117, 354
- Dodson-Robinson, S. E., & Salyk, C. 2011, *ApJ*, 738, 131
- Dong, R. 2015, *ApJ*, 810, 6
- Dong, R., & Dawson, R. 2016, *ApJ*, 825, 77
- Dong, R., et al. 2012a, *ApJ*, 760, 111

- . 2012b, *ApJ*, 750, 161
- Dong, R., Zhu, Z., & Whitney, B. 2015, *ApJ*, 809, 93
- Duffell, P. C. 2015, *ApJ*, 807, L11
- Duffell, P. C., & Dong, R. 2015, *ApJ*, 802, 42
- Dullemond, C. P. 2002, *A&A*, 395, 853
- Dullemond, C. P., & Dominik, C. 2004, *A&A*, 421, 1075
- Espaillet, C., Calvet, N., D’Alessio, P., Hernández, J., Qi, C., Hartmann, L., Furlan, E., & Watson, D. M. 2007, *ApJ*, 670, L135
- Espaillet, C., Calvet, N., Luhman, K. L., Muzerolle, J., & D’Alessio, P. 2008, *ApJ*, 682, L125
- Espaillet, C., D’Alessio, P., Hernández, J., et al. 2010, *ApJ*, 717, 441
- Espaillet, C., et al. 2014, ArXiv e-prints
- Flaherty, K. M., Hughes, A. M., Rosenfeld, K. A., Andrews, S. M., Chiang, E., Simon, J. B., Kerzner, S., & Wilner, D. J. 2015, *ApJ*, 813, 99
- Fukagawa, M., et al. 2013, *PASJ*, 65, L14
- Fung, J., & Chiang, E. 2016, ArXiv e-prints
- Fung, J., Shi, J.-M., & Chiang, E. 2014, *ApJ*, 782, 88
- Garufi, A., et al. 2013, *A&A*, 560, A105
- Garufi, A., Quanz, S. P., Schmid, H. M., Avenhaus, H., Buenzli, E., & Wolf, S. 2014, *A&A*, 568, A40
- Hashimoto, J., et al. 2012, *ApJ*, 758, L19
- . 2015, *ApJ*, 799, 43
- Isella, A., Pérez, L. M., Carpenter, J. M., Ricci, L., Andrews, S., & Rosenfeld, K. 2013, *ApJ*, 775, 30
- Jarrett, T. H., et al. 2011, *ApJ*, 735, 112
- Kenyon, S. J., & Hartmann, L. 1987, *ApJ*, 323, 714

- Kim, S.-H., Martin, P. G., & Hendry, P. D. 1994, *ApJ*, 422, 164
- Kley, W., & Nelson, R. P. 2012, *ARA&A*, 50, 211
- Lin, D. N. C., & Papaloizou, J. C. B. 1993, in *Protostars and Planets III*, ed. E. H. Levy & J. I. Lunine, 749–835
- Mathews, G. S., Williams, J. P., & Ménard, F. 2012, *ApJ*, 753, 59
- Mathis, J. S. 1990, *ARA&A*, 28, 37
- Mayama, S., et al. 2012, *ApJ*, 760, L26
- McMullin, J. P., Waters, B., Schiebel, D., Young, W., & Golap, K. 2007, in *Astronomical Society of the Pacific Conference Series*, Vol. 376, *Astronomical Data Analysis Software and Systems XVI*, ed. R. A. Shaw, F. Hill, & D. J. Bell, 127
- Miotello, A., Testi, L., Lodato, G., Ricci, L., Rosotti, G., Brooks, K., Maury, A., & Natta, A. 2014, *A&A*, 567, A32
- Moshir, M. 1989, *IRAS Faint Source Survey*, Explanatory supplement version 1 and tape
- Owen, J. E. 2016, *PASA*, 33, e005
- Owen, J. E., & Clarke, C. J. 2012, *MNRAS*, 426, L96
- Owen, J. E., Ercolano, B., & Clarke, C. J. 2011, *MNRAS*, 412, 13
- Owen, J. E., Ercolano, B., Clarke, C. J., & Alexander, R. D. 2010, *MNRAS*, 401, 1415
- Pascucci, I., et al. 2011, *ApJ*, 736, 13
- Pecaut, M. J., Mamajek, E. E., & Bubar, E. J. 2012, *ApJ*, 746, 154
- Pérez, L. M., Isella, A., Carpenter, J. M., & Chandler, C. J. 2014, *ApJ*, 783, L13
- Pinilla, P., Benisty, M., & Birnstiel, T. 2012a, *A&A*, 545, A81
- Pinilla, P., Birnstiel, T., Ricci, L., Dullemond, C. P., Uribe, A. L., Testi, L., & Natta, A. 2012b, *A&A*, 538, A114
- Pinilla, P., et al. 2015, *A&A*, 584, L4
- Preibisch, T., Brown, A. G. A., Bridges, T., Guenther, E., & Zinnecker, H. 2002, *AJ*, 124, 404

- Preibisch, T., & Zinnecker, H. 1999, *AJ*, 117, 2381
- Quanz, S. P., Avenhaus, H., Buenzli, E., Garufi, A., Schmid, H. M., & Wolf, S. 2013, *ApJ*, 766, L2
- Rau, U., & Cornwell, T. J. 2011, *A&A*, 532, A71
- Rice, W. K. M., Armitage, P. J., Wood, K., & Lodato, G. 2006, *MNRAS*, 373, 1619
- Rosenfeld, K. A., Chiang, E., & Andrews, S. M. 2014, *ApJ*, 782, 62
- Simon, J. B., Hughes, A. M., Flaherty, K. M., Bai, X.-N., & Armitage, P. J. 2015, *ApJ*, 808, 180
- Skrutskie, M. F., Dutkevitch, D., Strom, S. E., Edwards, S., Strom, K. M., & Shure, M. A. 1990, *AJ*, 99, 1187
- Strom, K. M., Strom, S. E., Edwards, S., Cabrit, S., & Skrutskie, M. F. 1989, *AJ*, 97, 1451
- Suzuki, T. K., Muto, T., & Inutsuka, S.-i. 2010, *ApJ*, 718, 1289
- Tamura, M. 2009, in *American Institute of Physics Conference Series*, Vol. 1158, American Institute of Physics Conference Series, ed. T. Usuda, M. Tamura, & M. Ishii, 11–16
- Tang, Y.-W., Guilloteau, S., Piétu, V., Dutrey, A., Ohashi, N., & Ho, P. T. P. 2012, *A&A*, 547, A84
- Thalmann, C., et al. 2010, *ApJ*, 718, L87
- Tsukagoshi, T., et al. 2014, *ApJ*, 783, 90
- van der Marel, N., Pinilla, P., Tobin, J., van Kempen, T., Andrews, S., Ricci, L., & Birnstiel, T. 2015a, *ApJ*, 810, L7
- van der Marel, N., van Dishoeck, E. F., Bruderer, S., Andrews, S. M., Pontoppidan, K. M., Herczeg, G. J., van Kempen, T., & Miotello, A. 2016, *A&A*, 585, A58
- van der Marel, N., et al. 2013, *Science*, 340, 1199
- van der Marel, N., van Dishoeck, E. F., Bruderer, S., Pérez, L., & Isella, A. 2015b, *A&A*, 579, A106
- van der Marel, N., van Dishoeck, E. F., Bruderer, S., & van Kempen, T. A. 2014, *A&A*, 563, A113

Whitney, B. A., Robitaille, T. P., Bjorkman, J. E., Dong, R., Wolff, M. J., Wood, K., & Honor, J. 2013, *ApJS*, 207, 30

Zacharias, N., Monet, D. G., Levine, S. E., Urban, S. E., Gaume, R., & Wycoff, G. L. 2005, *VizieR Online Data Catalog*, 1297

Zhang, K., Isella, A., Carpenter, J. M., & Blake, G. A. 2014, *ApJ*, 791, 42

Zhu, Z., Nelson, R. P., Dong, R., Espaillat, C., & Hartmann, L. 2012, *ApJ*, 755, 6

Zhu, Z., Nelson, R. P., Hartmann, L., Espaillat, C., & Calvet, N. 2011, *ApJ*, 729, 47

| Line | Rest frequency (GHz) | Beam size(") | PA($^{\circ}$) | rms ^(a) (mJy/beam) | peak ^(a) (mJy/beam) |
|--|----------------------|--------------------|------------------|-------------------------------|--------------------------------|
| $^{12}\text{CO } 2 \rightarrow 1$ | 230.53800 | 0.27×0.23 | 59 | 10 | 226 |
| $^{13}\text{CO } 2 \rightarrow 1$ | 220.39868 | 0.28×0.24 | 58 | 11 | 168 |
| $\text{C}^{18}\text{O } 2 \rightarrow 1$ | 219.56036 | 0.28×0.24 | 58 | 11 | 106 |
| Continuum | 234.00000 | 0.24×0.21 | 61 | 0.11 | 4.0 |

Table 1: Properties of the ALMA observations. ^(a) Measured in 0.25 km/s bins.

| | Gas | Small Dust | Big Dust |
|-------------------------------|------------|------------|----------|
| Total Mass (M_{J}) | 2.5 | 0.013 | 0.066 |
| R_{c} (AU) | 30 | 100 | 30 |
| R_{out} (AU) | 300 | 200 | 300 |
| γ | 1.0 | 2.0 | 1.0 |
| ψ | 0.5 | 1.1 | 0.5 |
| R_{cav} (AU) | $15^{(a)}$ | 60 | 70 |
| δ_{cav} | 10^{-5} | 0 | 0 |

Table 2: Parameters of the fiducial model. The last two parameters (R_{cav} and δ_{cav}) are varied in Section 4. ^(a) The gas surface density starts to decrease at 70 AU and reaches a minimum at 15 AU — see equation (4) and Figure 3.

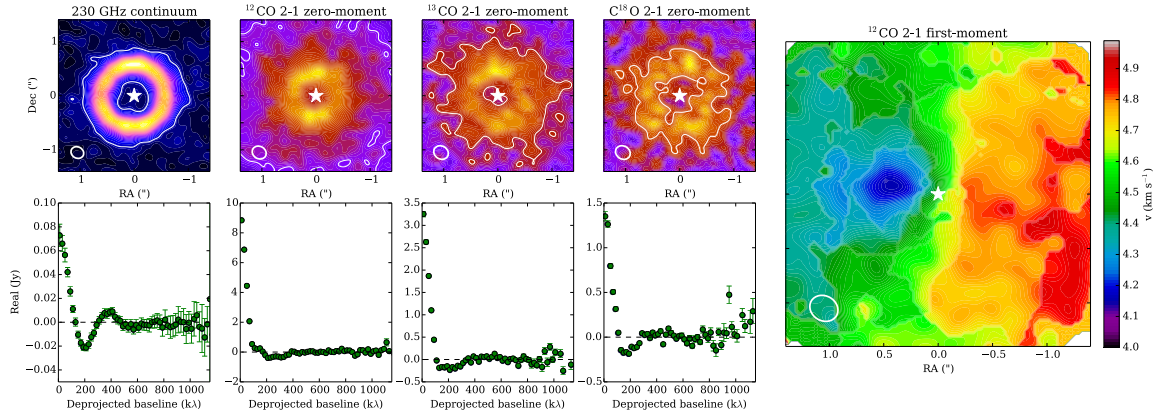


Fig. 1.— ALMA observations of the 230 GHz continuum, ^{12}CO , ^{13}CO and C^{18}O $J=2-1$ moment maps and visibility curves of J1604-2130. The zero-moment map is the total intensity, and the first-moment map is the velocity field. The 3σ contours are given in white, with $\sigma_{\text{continuum}}=0.11$ mJy and $\sigma_{\text{line}}=11$ mJy km s^{-1} for the integrated line emission.

Table 3: Archival SED data for J160421.7-213028

| Wavelength | F_ν (mJy) | Note |
|--|-----------------|---------------------------------------|
| $B^{a,b}$ | 64.6 | Preibisch & Zinnecker (1999) |
| $V^{a,b}$ | 114.9 | Zacharias et al. (2005) |
| $R^{a,b}$ | 194.8 | Preibisch & Zinnecker (1999) |
| $I^{a,b}$ | 237.6 | Preibisch & Zinnecker (1999) |
| 2MASS (J) ^{a,b} | 216.0 ± 4.6 | Cutri et al. (2003) |
| 2MASS (H) ^{a,b} | 275.0 ± 6.1 | Cutri et al. (2003) |
| 2MASS (K_s) ^{a,b} | 292.0 ± 5.6 | Cutri et al. (2003) |
| WISE (3.4 μm) ^b | 293.4 ± 5.9 | Cutri (2012) |
| WISE (4.6 μm) ^b | 251.0 ± 4.2 | Cutri (2012) |
| WISE (12 μm) ^b | 61.5 ± 0.8 | Cutri (2012) |
| WISE (22 μm) ^b | 152.1 ± 3.4 | Cutri (2012) |
| IRAC (4.5 μm) | 62.7 ± 0.8 | Carpenter et al. (2006) |
| IRAC (8.0 μm) | 26.3 ± 0.2 | Carpenter et al. (2006) |
| IRAC (16.0 μm) | 26.8 ± 0.2 | Carpenter et al. (2006) |
| IRAS (25 μm) | 273.2 ± 60.1 | Moshir (1989) |
| IRAS (60 μm) | 2754 ± 170.7 | Moshir (1989) |
| IRAS (100 μm) | 4355 ± 1045.2 | Moshir (1989) |
| AKARI (140 μm) | 5288.7 ± 1000.0 | VizieR II/298 |
| 880 μm | 164 ± 6 | Mathews et al. (2012) |
| 1.2 mm | 67.5 ± 1.4 | Mathews et al. (2012) |
| 2.6 mm | 5.1 ± 0.5 | Mathews et al. (2012) |
| IRS | — | Spitzer Heritage Archive ^c |

^aThe extinction law was adopted from Mathis (1990), assuming $A_v = 1$ for J1604 (Preibisch et al. 2002).

^bAbsolute flux conversions in optical, 2MASS, WISE photometric data were adopted from Bessell et al. (1998), Cohen et al. (2003), and Jarrett et al. (2011), respectively.

^cThis work is based in part on observations made with the Spitzer Space Telescope, obtained from the NASA/IPAC Infrared Science Archive, both of which are operated by the Jet Propulsion Laboratory, California Institute of Technology under a contract with the National Aeronautics and Space Administration.

| Component | R_{cav} (AU) | δ_{cav} |
|------------|-----------------------|------------------------|
| Small Dust | 60 ± 5 | $\lesssim 10^{-3}$ |
| Big Dust | 70 ± 10 | $\lesssim 10^{-3}$ |
| Gas | 15 ± 10 | $10^{-6} \sim 10^{-4}$ |

Table 4: Constraints on the cavity depth and radius in the three disk components assuming the cavity edge profiles are as in the fiducial model. See Section 4 for details.

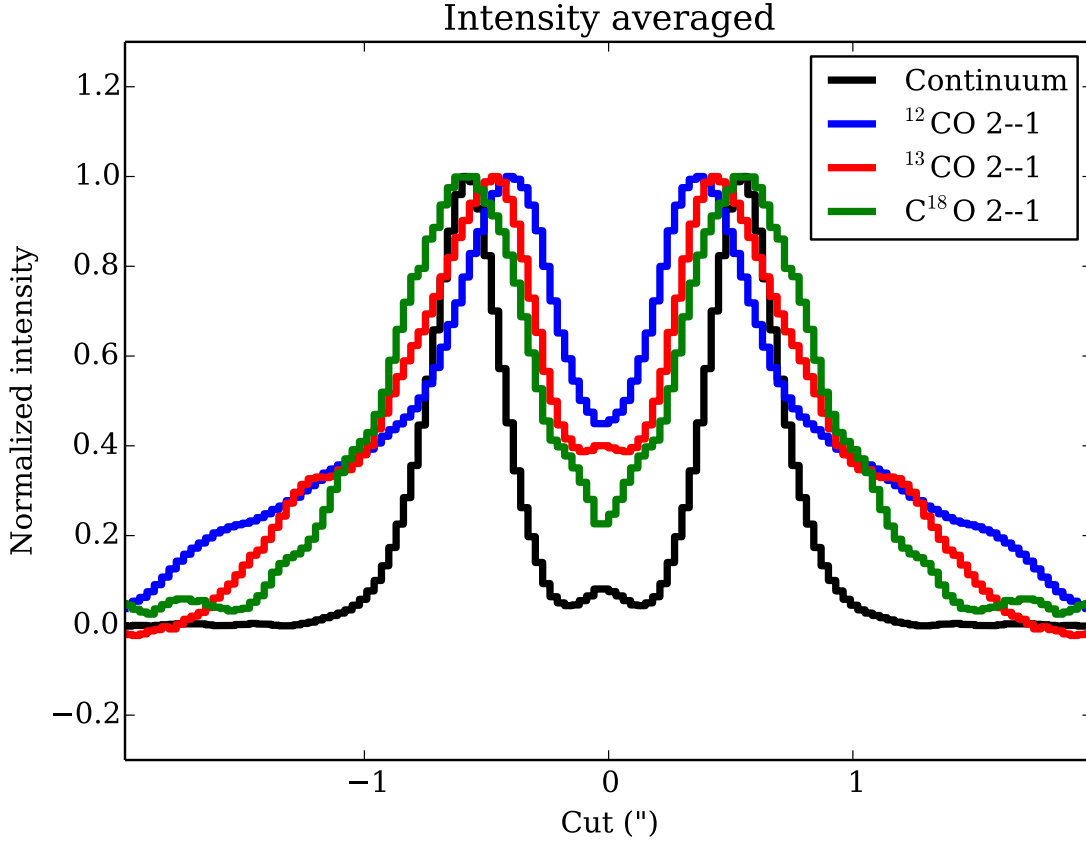


Fig. 2.— Azimuthally averaged normalized intensity of the ALMA observations of the 230 GHz continuum, ^{12}CO , ^{13}CO and C^{18}O $J = 2-1$ zero-moment maps of J1604-2130 from Figure 1.

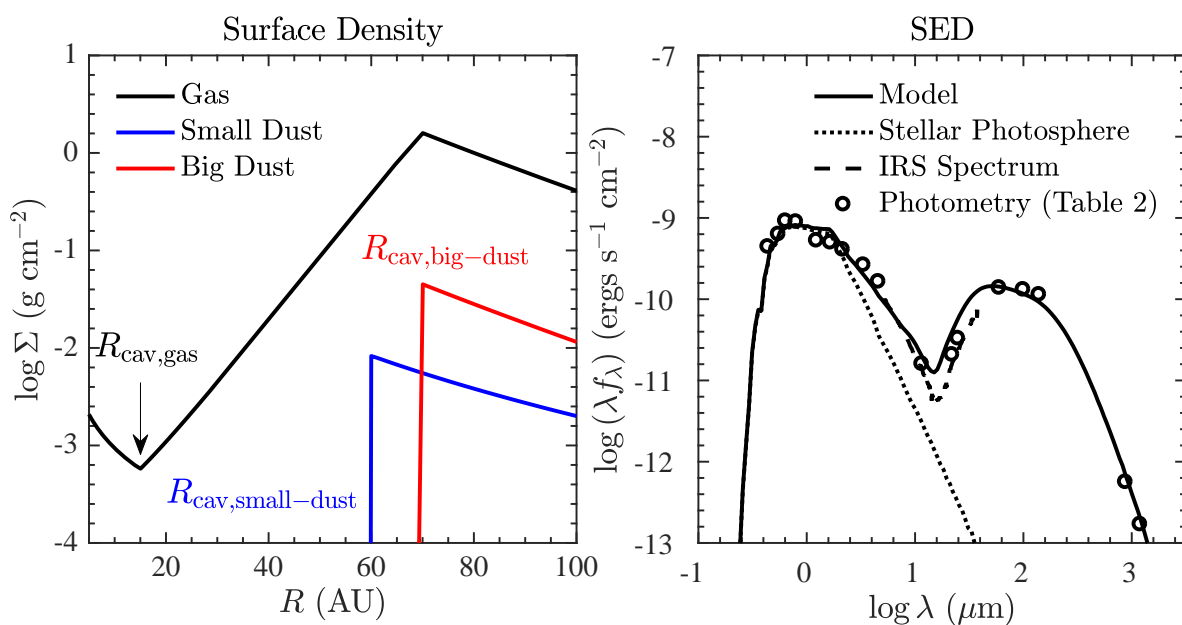


Fig. 3.— Surface density of each fiducial model component and the SED of the fiducial model. Observational data for the SED are listed in Table 3 (IRAC data points are ignored, see Section 4.1 for details).

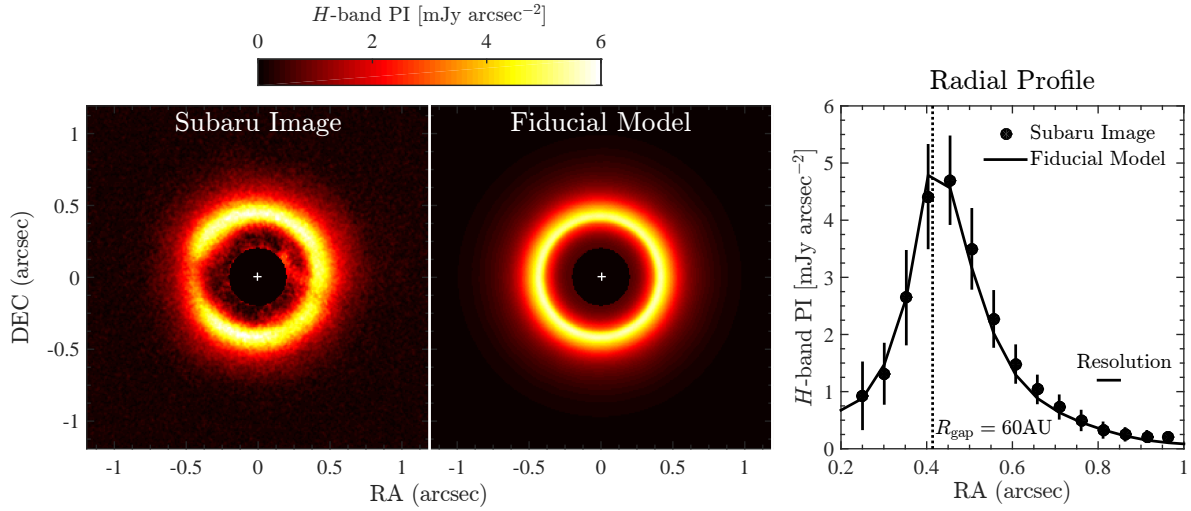


Fig. 4.— H -band polarized intensity comparison between the fiducial model and the observations (Mayama et al. 2012). The error bars in the radial profile represent the root mean square scatter of the pixels in each annulus in the Subaru image. The horizontal line segment in the right panel indicates the angular resolution in the Subaru observation.

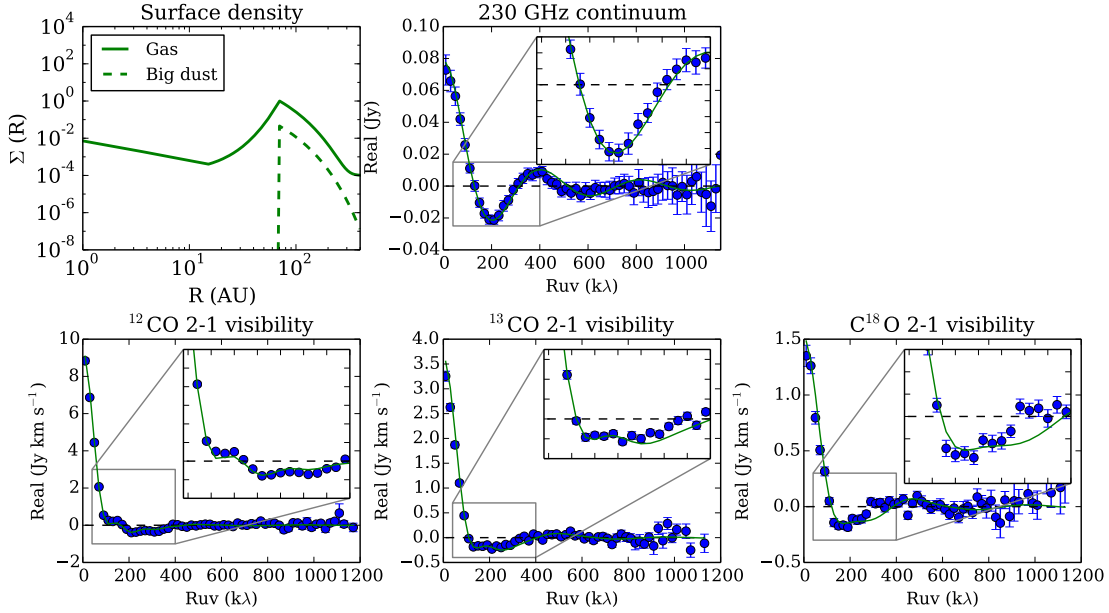


Fig. 5.— Visibilities of the fiducial model, compared with the observations. All visibility data have been binned to $20 \text{ k}\lambda$ and deprojected. The data are shown in blue circles with corresponding error bars and the model as green lines. A black dashed line indicates the null line. An inset shows a blow-up of the profile around the location of the null. **Top left:** The surface density profile of gas (solid) and big dust (dashed). **Top middle:** Visibility profile of the 230 GHz continuum. **Bottom left:** Integrated ^{12}CO 2-1 visibility profile. **Bottom middle:** Integrated ^{13}CO 2-1 visibility profile. **Bottom right:** Integrated C^{18}O 2-1 visibility profile. The model with the smooth density drop fits the data properly.

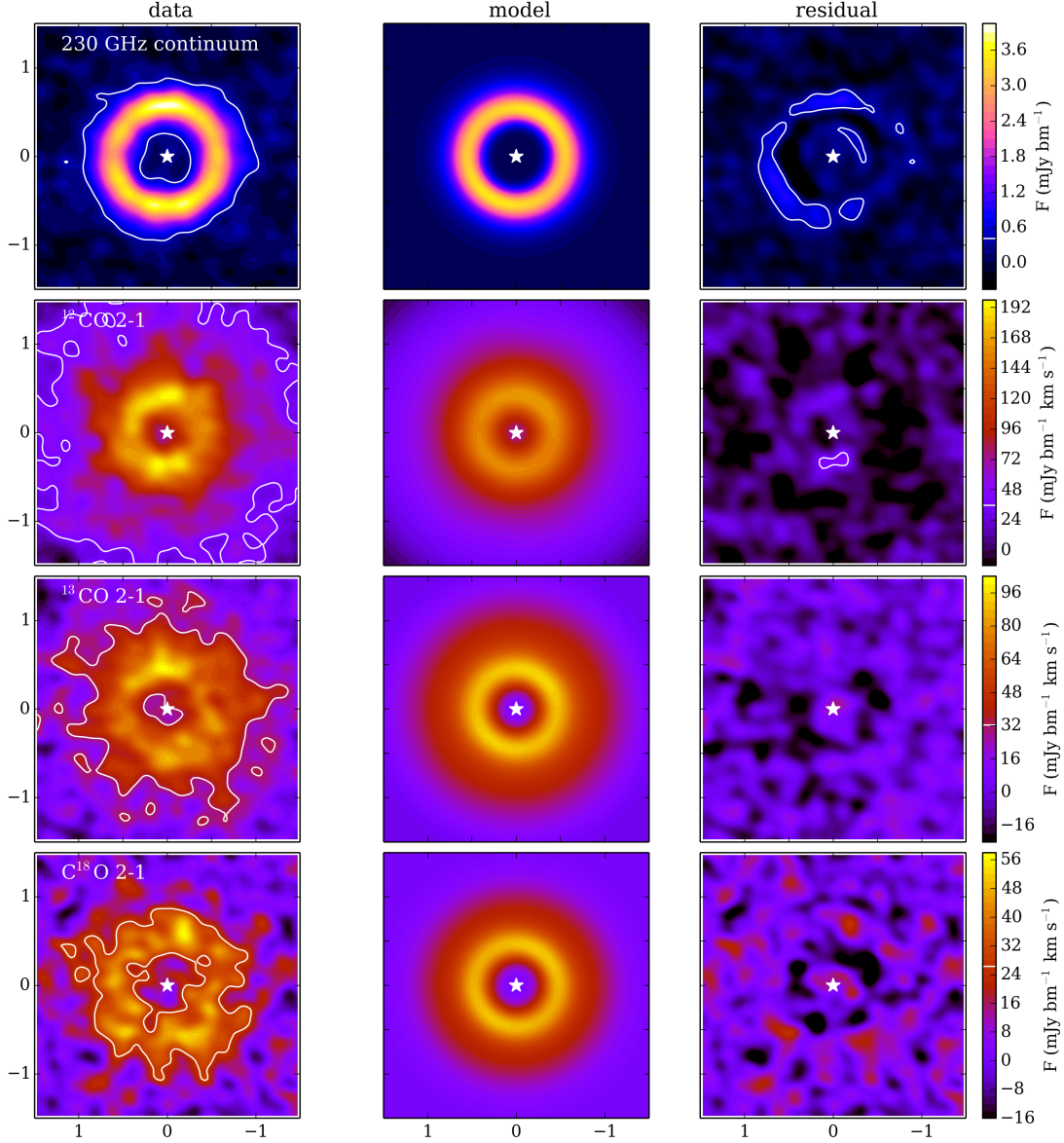


Fig. 6.— The fiducial model compared with the observations at mm wavelengths. Top to bottom shows the 230 GHz continuum, and the zero-moment maps of ^{12}CO 2-1, ^{13}CO 2-1, and C^{18}O 2-1. Each row shows (from left to right) the data, the model and the residuals (produced by inversely transform the data–model residuals in the Fourier space back to the image space) on the same color scale. The 3σ contours are given in white, with $\sigma_{\text{continuum}}=0.11$ mJy and $\sigma_{\text{line}} \approx 11$ mJy km s $^{-1}$ for the integrated line emission.

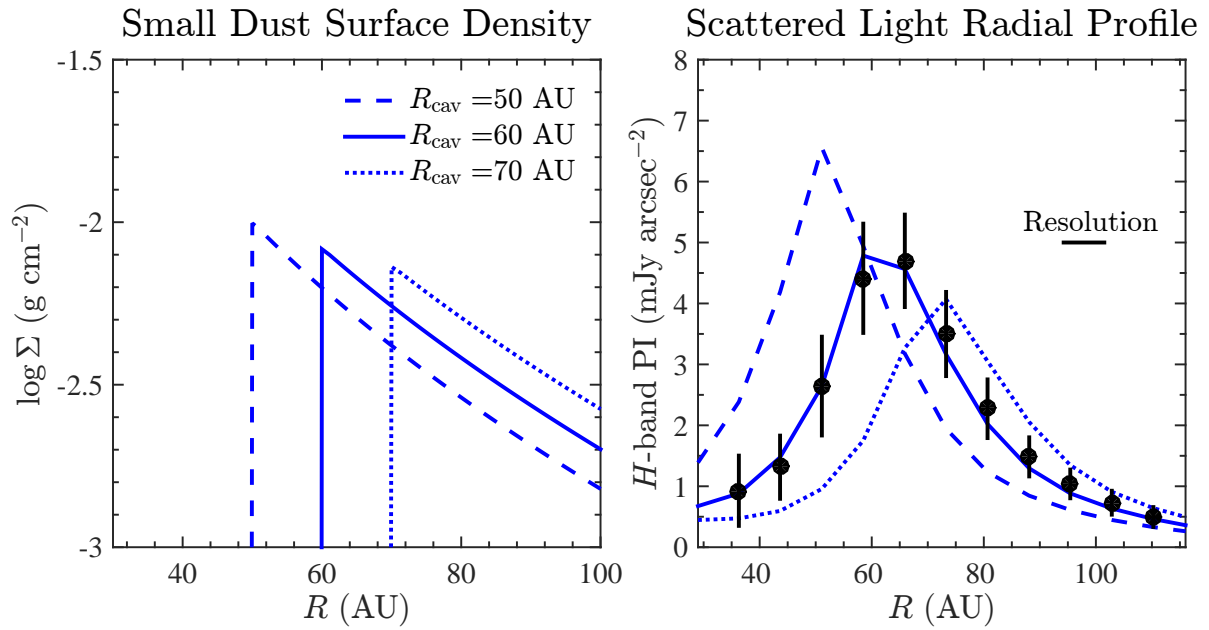


Fig. 7.— The effect of varying R_{cav} in small dust on the scattered light image.

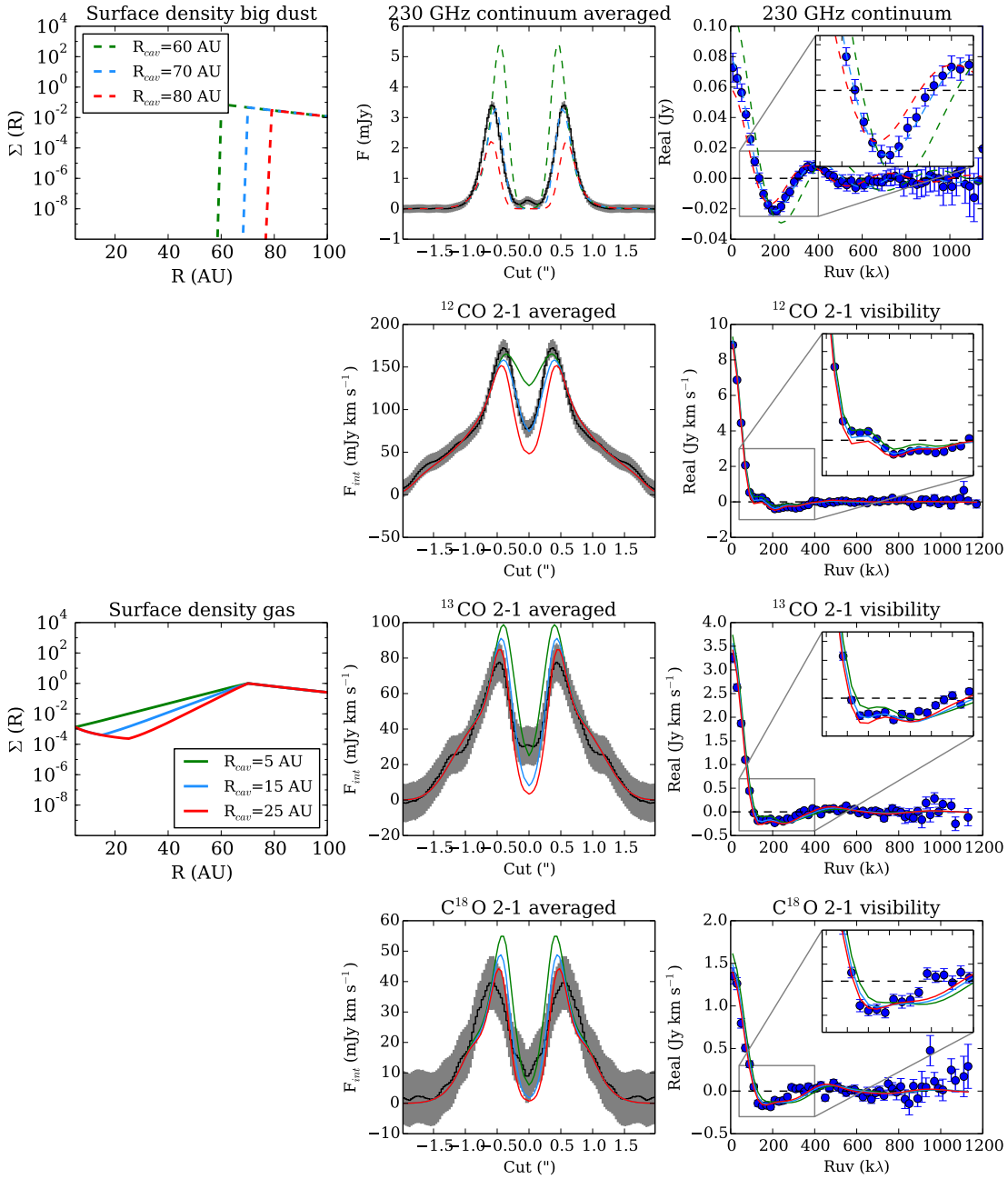


Fig. 8.— Modeling results for different cavity sizes. The two panels in the left column show the surface density variations, the middle column shows the azimuthally averaged intensity cuts (the noise level is indicated by the gray zone; the model images have the same beam as the ALMA observations), and the right column shows the visibility profiles. **Top to bottom in the middle and right columns:** (1st row) the 230 GHz continuum, (2nd row) the zero-moment maps of ^{12}CO 2-1, (3rd row) ^{13}CO 2-1, and (4th row) C^{18}O 2-1. The cavity sizes for the continuum are 60, 70 and 80 AU in green, blue, and red, respectively; and the gas cavity sizes are 5, 15 and 25 AU in green, blue, and red, respectively.

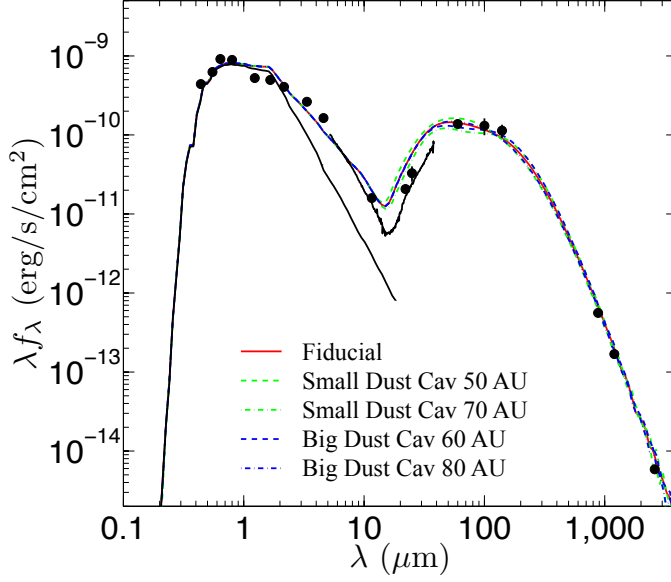


Fig. 9.— The effect of varying the cavity sizes in the dust on the SED.

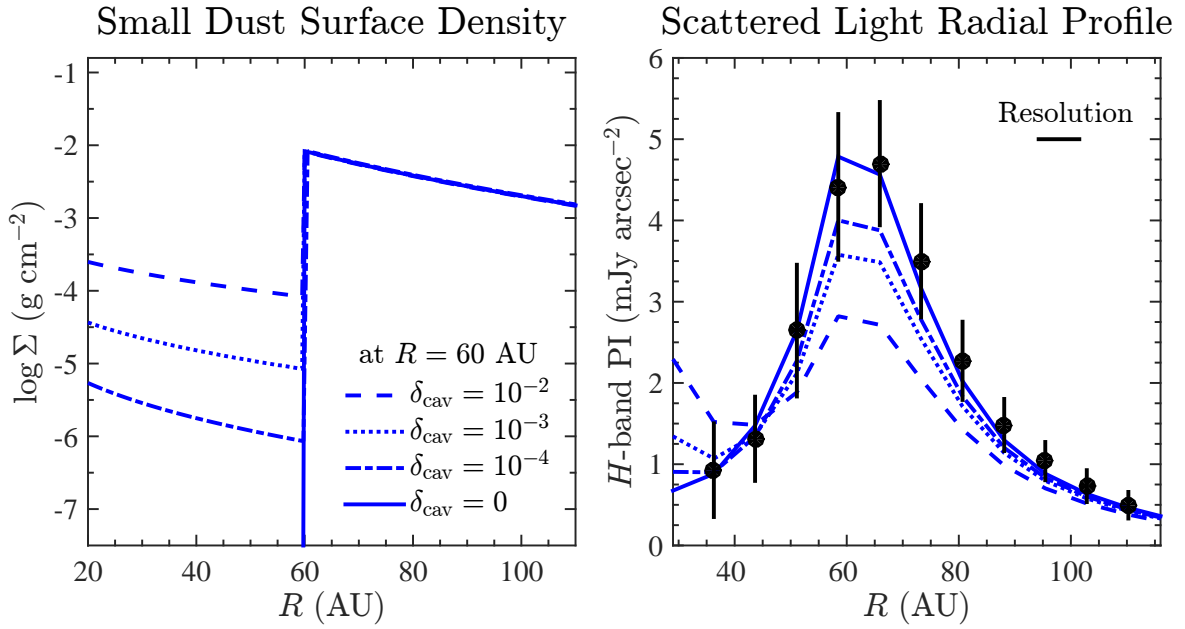


Fig. 10.— The effect of varying δ_{cav} in the small dust distribution.

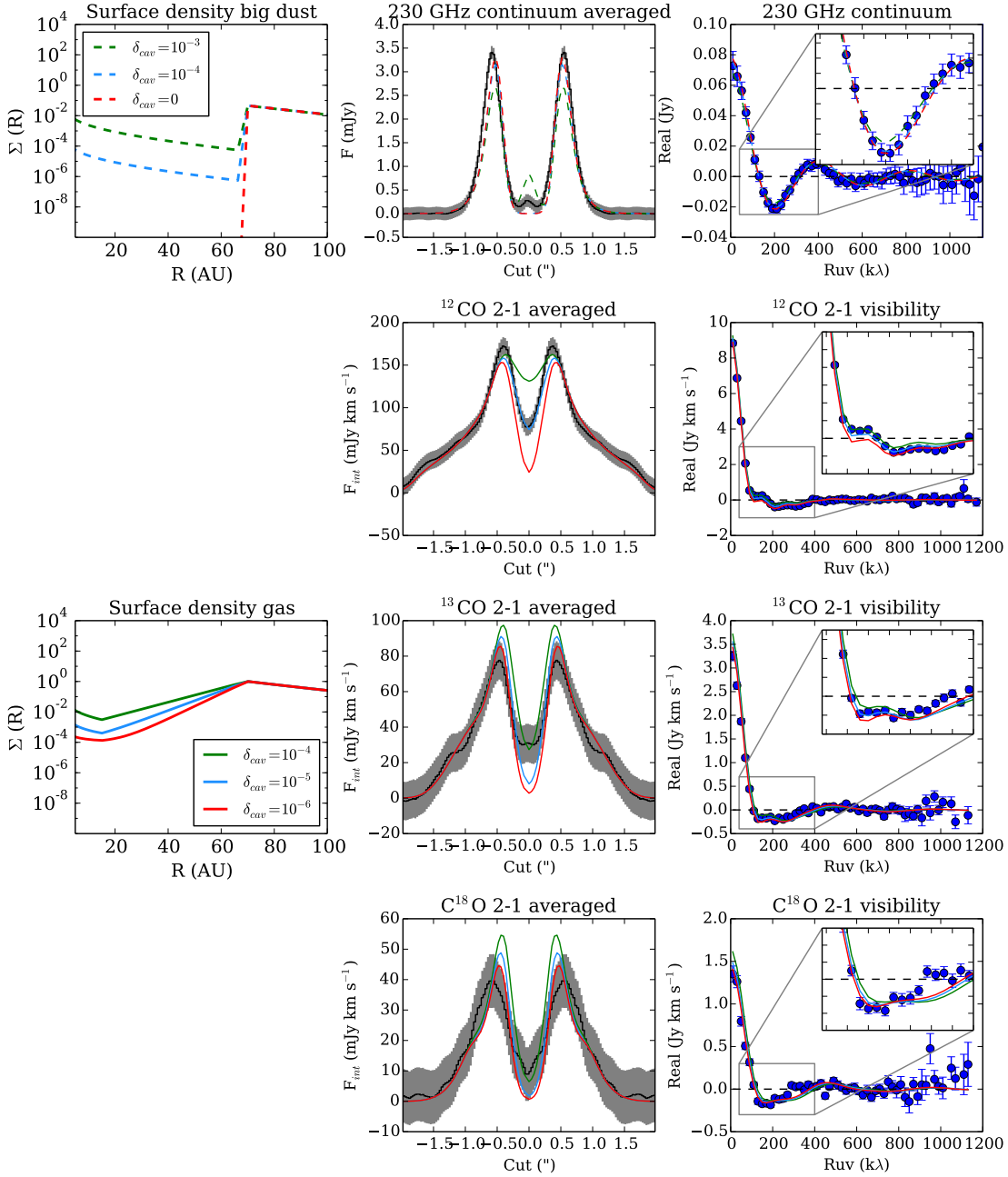


Fig. 11.— Modeling results for different cavity depths in the gas density. The two panels in the left column show the surface density variations, the middle column shows the azimuthally averaged intensity cuts (the noise level is indicated by the gray zone; the model images have the same beam as the ALMA observations), and the right column shows the visibility profiles. **Top to bottom in the middle and right columns:** (1st row) the 230 GHz continuum, (2nd row) the zero-moment maps of ^{12}CO 2-1, (3rd row) ^{13}CO 2-1, and (4th row) C^{18}O 2-1, with depths of 10^{-4} , 10^{-5} , and 10^{-6} . In the dust surface density, green, blue, red curves are for 10^{-3} , 10^{-4} , and infinite depletion, respectively.

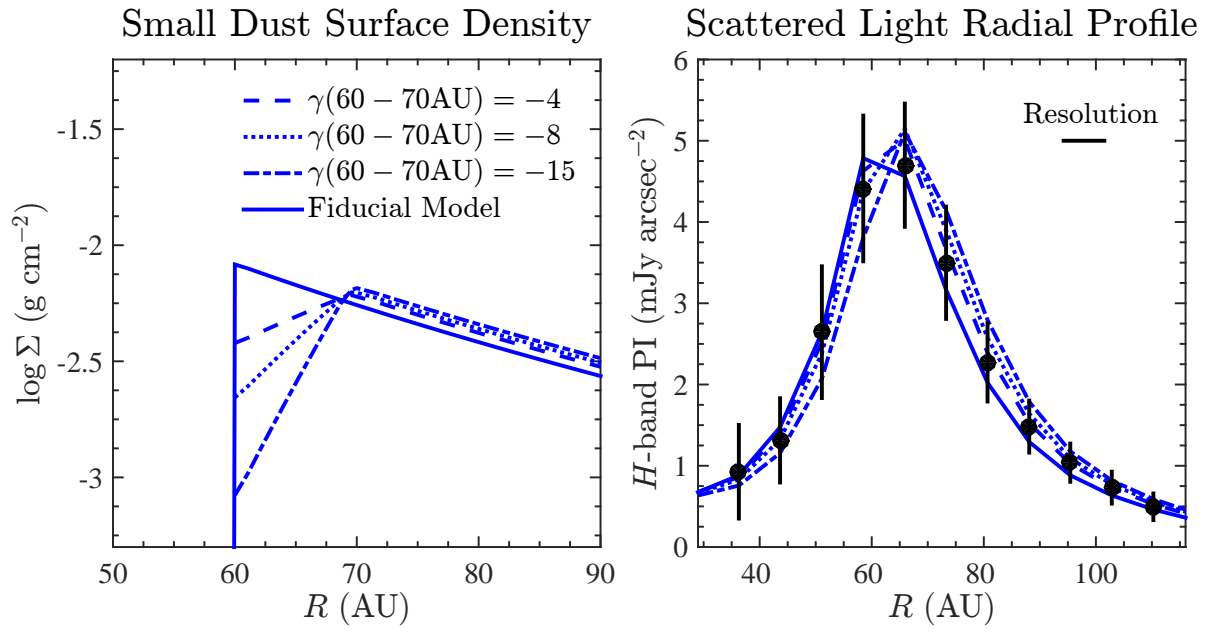


Fig. 12.— The effect of a smooth cavity edge transition between 60 AU and 70 AU in the small dust on the scattered light image.

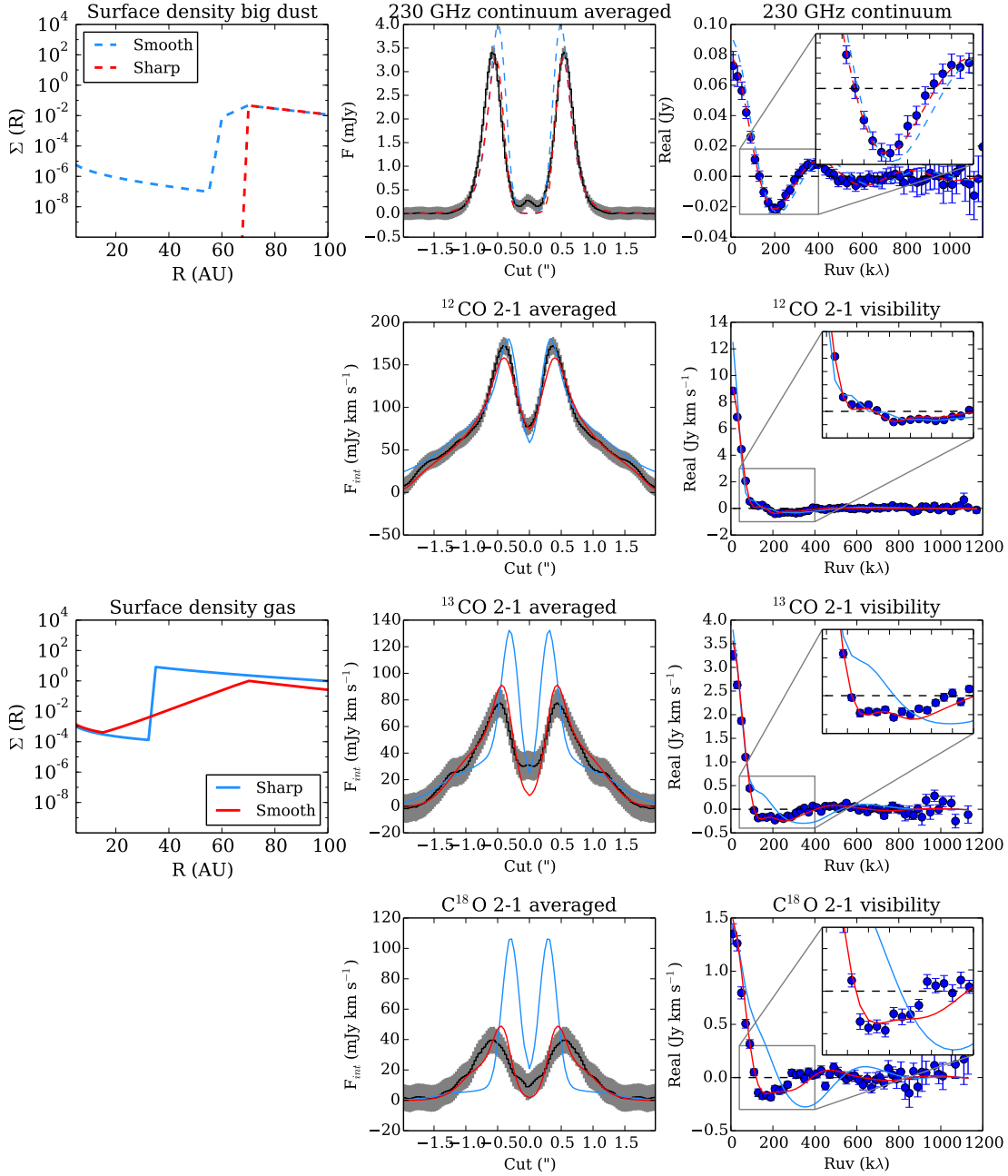


Fig. 13.— Modeling results for sharp vs. smooth density drops in gas and in big dust (such as used in van der Marel et al. 2015b) compared with observations. The two panels in the left column show the surface density variations, the middle column shows the azimuthally averaged intensity cuts (the noise level is indicated by the gray zone; the model images have the same beam as the ALMA observations), and the right column shows the visibility profiles. **Top to bottom in the middle and right columns:** (1st row) the 230 GHz continuum, (2nd row) the zero-moment maps of ^{12}CO 2-1, (3rd row) ^{13}CO 2-1, and (4th row) C^{18}O 2-1.